A Comparison of Automatic Hand-Eye Calibration Methods for Vision-Guided Collaborative Robots

Fernando S. Braga*
Aeronautics Institute of Technology
Center of Competence in Manufacturing
São José dos Campos, Brazil
fernando.braga@ccm-ita.org.br
Corresponding Author*

Felipe C. Gomes
Aeronautics Institute of Technology
Center of Competence in Manufacturing
São José dos Campos, Brazil
felipe.gomes@ccm-ita.org.br

Wesley R. Oliveira
Aeronautics Institute of Technology
Center of Competence in Manufacturing
São José dos Campos, Brazil
wesleyro@ccm-ita.org.br

***Abstract*—This paper revisits the well-known robotics problem of hand–eye calibration under the eye-in-hand interpretation, in which a camera (eye) is rigidly attached to the end-effector (hand) of a collaborative robot arm (COBOT). Classically, the problem consists of solving $AX = XB$ to estimate the transformation X between hand and camera frames, given the relative successive pose changes of the hand (A) and camera (B) coordinate frames. We experimentally compare three state-of-the-art hand–eye calibration methods: Tsai–Lenz (1989), Park–Martin (1994), and XC2 (2019), using a fully automated pipeline in a task-level visual servoing application where the robot is repeatedly positioned using vision feedback. The experiments evaluate the effect of different illumination levels under controlled industrial conditions. Results are statistically analyzed using common robot positioning metrics, including accuracy and repeatability, and conclusions are drawn regarding the most stable operating conditions for reliable automatic hand–eye calibration in industrial robotic systems.**

***Index Terms*—Hand-Eye Calibration, Automatic Camera Calibration, Industrial Robots, Robotic Vision.**

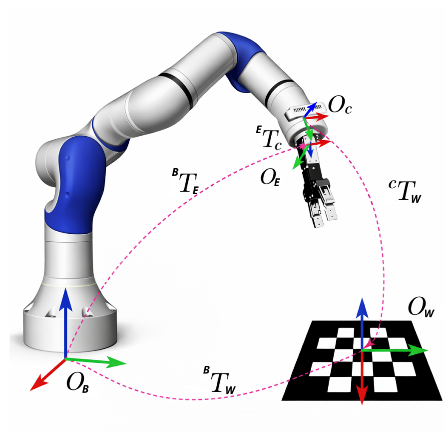

Fig. 1: Illustrative robot vision cell with eye-in-hand approach: a camera (eye) mounted at the hand of a robot.

I. Introduction

Hand-eye calibration underpins vision-based robot control, such as visual servoing, where camera feedback directs motion for tasks such as grasping, inspection, and pick-and-place [1]–[3]. As illustrated in Fig.1, it involves estimating the homogeneous transformation that links the robot's hand frame to the optical frame of a camera mounted on it, so that sensor measurements can be combined with the arm's pose and expressed in the robot base coordinate system (C.S.) [1].

Accurate spatial registration is fundamental for converting sensor data into reliable coordinates in robotic automation. This problem has been extensively addressed in robotics and computer vision, with numerous calibration techniques for 2D RGB and depth sensors [2], [4]–[8]. Motion-based hand–eye calibration can run automatically [4], as illustrated in Fig. 2.

Seminal contributions by Tsai and Lenz [6] and Shiu and Ahmad [7] introduced the separable hand–eye solution, estimating rotation and translation independently; Tsai–Lenz remains a widely used benchmarking approach with checkerboard calibration and is adopted in this paper. Reference [1] analyzes objective functions based on pose or reprojection error under the 'hand–eye' and 'robot–world–hand–eye' formulations, and, building on the nonlinear optimization framework of [5], proposes XC2, a full-pose simultaneous solution computed via Levenberg–Marquardt.

This work was supported by the São Paulo Research Foundation (FAPESP) under Project FLYMOV (Grant No. 2021/11258-5).

Despite these advances, hand–eye calibration remains sensitive to algorithm parameters, lighting conditions, and target placement, where small variations can degrade camera–robot transformation estimates and motion accuracy. Moreover, classical 2D RGB approaches often require substantial human intervention and are typically validated with few trials, providing limited analysis of task-level accuracy and lighting effects.

This paper addresses these limitations by presenting a practical experimental comparison of the Tsai–Lenz [6], Park–Martin [9], and XC2 [1] methods through a fully automated pipeline. After each automatic calibration (Fig. 2), a task-level visual servoing goal is executed using AprilTag-marked targets [10], whose detected positions are fed to the robot position control loop. The task is repeated with five targets under three industrial lighting conditions. System performance is quantified using adapted ISO manipulator positioning metrics [11], including positioning accuracy and

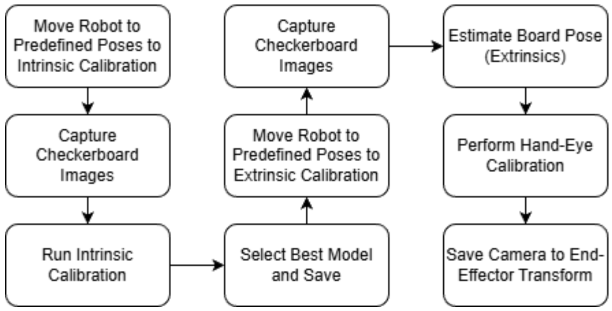

Fig. 2: Classical automated workflow for hand-eye calibration.

repeatability, and the results are statistically compared via ANOVA [12] to identify the most reliable automatic hand–eye calibration approach under variable illumination.

This paper is organized as follows: Section II presents the mathematical and algorithmic background of the robot vision calibration framework; Section III describes the methodology; Section IV reports the results and discussion; and Section V concludes the paper.

II. Background

This section briefly reviews the main calibration procedures in a robot vision system. It first outlines the concepts and parameters of intrinsic calibration required to map image-pixel features into the camera metric coordinate system via perspective transformation [13], and then revisits the hand–eye calibration problem, defined by the coordinate system relationships illustrated in Fig. 1.

A. Intrinsic Calibration

The camera is assumed to follow the classical pinhole projection model with radial and tangential distortion [14], [15]. Let $\mathbf{K}$ denote the intrinsic matrix parameter,

$$\mathbf{K} = \begin{bmatrix} f_x & 0 & c_x \\ 0 & f_y & c_y \\ 0 & 0 & 1 \end{bmatrix}, \tag{1}$$

where f_x and f_y are the focal lengths and (c_x, c_y) is the principal point. Radial distortion coefficients (k_1, k_2, k_3) and tangential distortion coefficients (p_1, p_2) were considered. Intrinsic calibration involves solving an optimization problem to determine these parameters. It is performed prior to any hand-eye computation in this work.

This paper uses the Camera Calibrator Toolbox® from MATLAB 2024b. A planar checkerboard pattern (5 × 8 inner corners) was rigidly fixed in the robot workspace (calibrator in Fig.1). Photographs of the pattern from multiple viewpoints are taken with the camera to be used in the investigations: the RGB sensor of an Intel® RealSense D435, with a resolution of 640 x 480 pixels. A total of 15 images were automatically acquired from spatially distinct robot poses, ensuring variation in orientation, distance, and field-of-view coverage. This diversity is necessary to avoid parameter correlation and to improve numerical conditioning during intrinsic estimation.

Intrinsic calibration is based on the RMS reprojection error, Eq. 2, which is defined as the Euclidean distance between feature points detected over the pattern and projected model points after optimization [14].

$$e_{\text{RMS}} = \sqrt{\frac{1}{N}\sum_{i=1}^{N} \|\mathbf{x}_i - \hat{\mathbf{x}}_i\|_2^2} \tag{2}$$

The final intrinsic model was chosen based on the minimum RMS reprojection error, ensuring consistency before proceeding to extrinsic estimation and hand-eye calibration. To improve robustness and avoid suboptimal calibration, an automated parameter selection routine was implemented. Different distortion configurations were evaluated, and the model yielding the lowest mean reprojection error (0.088 pixels) across all calibration images is selected. The calibration images and the selected intrinsic parameters used throughout this study are made available in the accompanying dataset in the directory [16].

B. Extrinsic Estimation and Hand-Eye Calibration

Departing from the perspective of the coordinate systems depicted in Figure 1, the basic hand-eye calibration problem is now reviewed. The coordinate systems involved are defined as follows:

- $\{B\}$: Robot base frame;
- $\{E\}$: Robot end-effector frame;
- $\{C\}$: Camera optical frame;
- $\{W\}$: Pattern frame (calibrator or AprilTag).

The primary goal of hand-eye calibration is to estimate the homogeneous transformation ${}^{E}\mathbf{T}_C$ which represents the pose of the camera with respect to the end-effector. Once obtained, this transformation enables expressing target poses/pattern (W) in the robot base frame through the chain:

$${}^{B}\mathbf{T}_W = {}^{B}\mathbf{T}_E\, {}^{E}\mathbf{T}_C\, {}^{C}\mathbf{T}_W \tag{3}$$

For each image, the pose of the checkerboard/target object relative to the camera frame, ${}^{C}\mathbf{T}_W$, is estimated using standard perspective-n-point (PnP) optimization based on the previously estimated intrinsic parameters [14]. In addition, the robot controller provides the end-effector pose relative to the robot base frame, ${}^{B}\mathbf{T}_E$. From successive robot motions, relative transformations between the robot base C.S. $\{B\}$ and the target/calibrator C.S. $\{W\}$ are to be fixed and computed as

$${}^{B}\mathbf{T}_W = ({}^{B}\mathbf{T}_{E,i})^{E}\mathbf{T}_C{}^{C,i}\mathbf{T}_W \tag{4}$$

$${}^{B}\mathbf{T}_W = ({}^{B}\mathbf{T}_{E,i+1})^{E}\mathbf{T}_C{}^{C,i+1}\mathbf{T}_W \tag{5}$$

And equalizing (4) and (5), it follows

$$({}^{B}\mathbf{T}_{E,i})^{E}\mathbf{T}_C{}^{C,i}\mathbf{T}_W = ({}^{B}\mathbf{T}_{E,i+1})^{E}\mathbf{T}_C{}^{C,i+1}\mathbf{T}_W \tag{6}$$

From which follows

$$({}^{B}\mathbf{T}_{E,i+1})^{-1}{}^{B}\mathbf{T}_{E,i}{}^{E}\mathbf{T}_{C} = {}^{E}\mathbf{T}_{C}{}^{C,i+1}\mathbf{T}_{W}({}^{C,i}\mathbf{T}_{W})^{-1} \quad (7)$$

And from (6) we define

$$\mathbf{A}_i = ({}^{B}\mathbf{T}_{E,i+1})^{-1}{}^{B}\mathbf{T}_{E,i} \quad (8)$$

and

$$\mathbf{B}_i = {}^{C,i+1}\mathbf{T}_{W}({}^{C,i}\mathbf{T}_{W})^{-1}. \quad (9)$$

The hand-eye problem is then formulated as in Eq. 10:

$$\mathbf{A}_i\mathbf{X} = \mathbf{X}\mathbf{B}_i, \quad (10)$$

where $X \in SE(3)$, $\mathbf{X} = {}^{E}\mathbf{T}_{C}$, is the unknown rigid transformation between the end-effector and the camera.

The three hand-eye solution methods evaluated in this paper are briefly reviewed below:

- XC2 [1]: a simultaneous nonlinear solution of Eq. 10, jointly estimating rotation and translation by minimizing a full-pose consistency error in $SE(3)$ through a nonlinear least-squares formulation solved via a Levenberg–Marquardt scheme with quaternion parameterization.
- Tsai-Lenz [6]: a classical linear method that decouples rotation and translation into two steps; rotation is first estimated from relative motion pairs via least squares, and translation is subsequently obtained from a secondary linear system, yielding computational efficiency and robustness under small to moderate noise.
- Park-Martin [9]: a Lie algebra-based approach mapping relative rotations to $SO(3)$ via the matrix logarithm, estimating rotation by solving a linear system in the tangent space for geometric consistency, followed by translation recovery through a linear formulation dependent on the estimated rotation.

In this paper, the XC2 [1] is implemented from the Matlab code made available by the authors from their referenced GitHub folder. The Tsai-Lenz [6] is used from the *estimateCameraRobotTransform* Matlab function available within the Robotics Systems Toolbox®. The Park-Martin [9] is implemented by the authors in Matlab. Each method estimates ${}^{E}\mathbf{T}_{C}$, which is subsequently used within the task-level visual servoing test procedure detailed in the next.

III. Methodology

The general paper workflow is illustrated in Fig. 3. The methodology aims to estimate the rigid transformation between the camera and robot end-effector frames and to evaluate the accuracy and repeatability of different hand–eye calibration methods under controlled conditions. It comprises three stages: camera intrinsic calibration; a fully automated pipeline for extrinsic estimation and hand–eye calibration using the aforementioned methods; and experimental evaluation in an industrial collaborative robotic cell (Fig. 4).

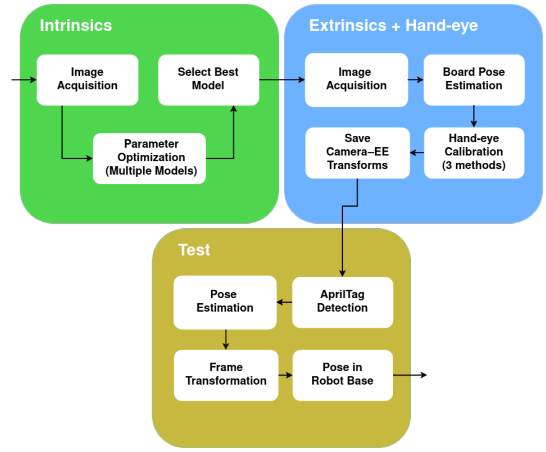

Fig. 3: Methodology flow, including intrinsic calibration, extrinsic and hand-eye calibration, and test procedures.

A. Experimental Setup

The experimental platform is shown in Fig. 4. It is defined to reproduce a generic task-level visual servoing test procedure, comprising the following components:

1) Robot: Universal Robots UR16e (nominal pose repeatability: ±0.05 mm).
2) Camera: Intel RealSense D435 RGB-D, rigidly mounted in eye-in-hand configuration via a 3D-printed support; only the RGB stream was used.
3) Calibration Pattern: Planar checkerboard (5 × 8 inner corners) for intrinsic and extrinsic calibration.
4) AprilTags [10]: Five tag36h11 markers (49 mm side length) fixed at known workspace positions.
5) Tool: Custom TCP with needle tip mounted on the flange for physical probing of each AprilTag center relative to $\{B\}$ prior to testing.
6) Illumination Measurement: Digital illuminance meter defining three conditions: Low (145 lx), Medium (243 lx), and High (352 lx).
7) External PC: Laptop (Intel i5 CPU, NVIDIA GTX1050 GPU, 16 GB RAM, Ubuntu 20.04) for robot control, image acquisition, calibration, and data analysis.

Robot motion control and image acquisition are automatically executed via a Python interface communicating with the UR16e manipulator through RTDE (Real-Time Data Exchange) and the Intel RealSense D435 camera. Calibration computations, homogeneous transformations, and statistical processing are performed in MATLAB. Once initialized, the procedure runs without human intervention, requiring only the placement of the AprilTag targets in the workspace.

B. Experimental Procedure

As illustrated in Fig. 3, distinct datasets were used to evaluate the robustness of the three hand-eye methods: intrinsic calibration was performed once using the checkerboard, while extrinsic and hand-eye estimation relied on 30 checkerboard images acquired at 30 distinct robot poses, ensuring sufficient

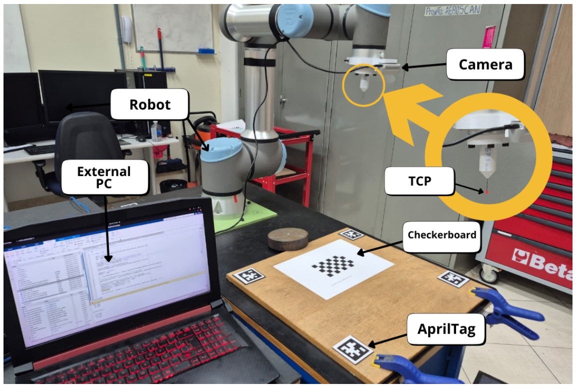

Fig. 4: Experimental setup for automatic hand–eye calibration, showing the camera view of the workspace with the UR16 robot, calibration checkerboard, five AprilTags, a tool with known TCP, and an Intel RealSense camera mounted near the robot flange.

rotational and translational diversity in $SE(3)$ and avoiding near-parallel motions that may cause ill-conditioning in Eq. 10. The experiments followed a block design combining calibration method and illumination level, yielding nine blocks (3 methods $\times$ 3 lighting conditions), with randomized block order and fixed factors within each block. Under each block, five workspace-distributed AprilTags were sequentially detected, and the visual servoing task was repeated 30 times per tag according to standardized repeatability guidelines, resulting in $9 \times 5 \times 30 = 1350$ trials. In each trial, the commanded robot position (RTDE) was compared with the ground-truth tag center obtained via TCP probing. Given that the AprilTags were fixed spatial targets and the objective was to evaluate global positioning performance, 30 measurements were collected per AprilTag under each illumination condition to compute the repeatability and accuracy of each method–illumination combination.

The individual Cartesian positioning error was defined as

$$e_k = \left\| \mathbf{p}_k - \mathbf{p}_{gt} \right\|, \tag{11}$$

where $\mathbf{p}_k$ denotes the estimated tag position at repetition k, and $\mathbf{p}_{gt}$ the corresponding ground-truth reference. In addition to individual trial error, positioning performance was evaluated according to ISO 9283, computing positional accuracy (A_p) and repeatability (R_p) for each target and experimental block over $n = 30$ repetitions. Positional accuracy is defined as the Euclidean distance between the mean measured position and the ground-truth reference:

$$A_p = \left\| \bar{\mathbf{p}} - \mathbf{p}_{gt} \right\|, \tag{12}$$

where

$$\bar{\mathbf{p}} = \frac{1}{n} \sum_{k=1}^{n} \mathbf{p}_k \tag{13}$$

denotes the mean estimated position.

For repeatability, the distance of each repetition to the barycenter is defined as

$$l_k = \left\| \mathbf{p}_k - \bar{\mathbf{p}} \right\|. \tag{14}$$

The mean distance is

$$\bar{l} = \frac{1}{n} \sum_{k=1}^{n} l_k, \tag{15}$$

and the corresponding standard deviation is

$$S_l = \sqrt{\frac{1}{n-1} \sum_{k=1}^{n} \left(l_k - \bar{l} \right)^2}. \tag{16}$$

According to ISO, positional repeatability is defined as

$$R_p = \bar{l} + 3S_l. \tag{17}$$

While A_p and R_p quantify systematic bias and dispersion, inferential analysis was performed using the log-transformed of A_p and R_p, from which block-level accuracy and repeatability metrics were derived for interpretation using the complete filtered dataset ($n = 1315$), obtained via MAD-based outlier removal ($k = 3.5$), with AprilTag modeled as a random effect to avoid pseudoreplication. Statistical independence between repetitions was promoted by returning the robot to a predefined home configuration between trials, with an average interval of approximately 4 s between each two successive trials.

C. Data Analysis

Using the acquired data, a two-way full-factorial design with interaction [12] is adopted to assess the effects of two factors: calibration method (XC2, Tsai-Lenz, and Park-Martin) and illumination level (Low, Medium, and High), as described by the statistical model in Eq. 18. The same model structure is employed twice in this study: first considering accuracy as the response variable and, separately, considering repeatability as the response variable.

$$\log\left(Y_{ijk}\right) = \mu + A_i + B_j + (AB)ij + \bar{u}_k + \varepsilon ijk \tag{18}$$

where the response variable log! (Y_{ijkl}) denotes the natural logarithm of the performance metric observed in each condition analyzed in the experiment (tag and block combination), obtained using the i-th calibration method under the j-th illumination condition and associated with the k-th AprilTag. In the first analysis, Y_{ijkl} represents the calibration accuracy error; in the second analysis, Y_{ijkl} represents the calibration repeatability error.

The fixed-effects structure comprises the overall mean μ, the main effect of calibration method A_i, the main effect of illumination B_j, and their interaction $(AB)_{ij}$, which capture systematic variations attributable to the experimental factors. The term u_k represents the random effect of the k-th AprilTag, accounting for tag-specific variability not explained by the fixed effects and assumed to follow a normal distribution,

$$\bar{u}_k \sim \mathcal{N}\left(0, \sigma^2_{\text{AprilTag}}\right), \tag{19}$$

reflecting random deviations around zero with variance $\sigma^2_{\text{AprilTag}}$. The residual error term ε_{ijkl} models the remaining unexplained variability and is assumed to be independently and identically distributed as

$$\varepsilon_{ijkl} \sim \mathcal{N}\left(0, \sigma^2\right). \tag{20}$$

The indices i, j, k, and l denote the calibration method, illumination level, AprilTag, and repeated trial, respectively. Following Montgomery [12], a logarithmic transformation is applied to the response variable to stabilize variance, mitigate right-skewness and heteroscedasticity, and improve residual normality for the ANOVA framework in both the accuracy and repeatability analyses.

The statistical analysis was performed in the *R* environment using a mixed-effects analysis of variance based on Eq. 18 to evaluate the main effects of calibration method and illumination, their interaction, and AprilTag-related variability via a random-effect term.

IV. Results and Discussion

The results section presents two independent analyses of variance addressing accuracy and repeatability. Both analyses are based on an initial dataset of 1350 measurements, filtered using a Median Absolute Deviation (MAD) criterion with $k = 3.5$, resulting in 1315 valid samples. Accuracy and repeatability were computed per method–illumination block, with AprilTag treated as a source of random variability.

Figures 5–8 summarize the distributions of the log-transformed accuracy and repeatability metrics across illumination levels and calibration methods.

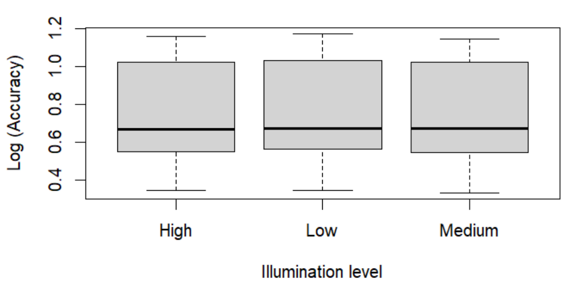

Fig. 5: Accuracy by illumination level (log-scale).

From a qualitative perspective, the boxplots indicate that illumination appears to influence repeatability more noticeably than accuracy. Whereas the accuracy distributions under different lighting conditions exhibit substantial overlap and only minor differences in median values (Fig. 5), the repeatability results show comparatively clearer variations across illumination levels (Fig. 6). This visual evidence suggests that lighting conditions tend to affect variability more strongly than systematic error.

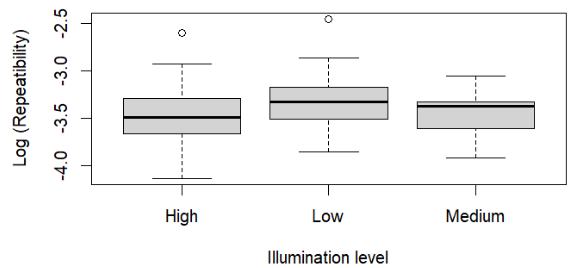

Fig. 6: Repeatability by illumination level (log-scale).

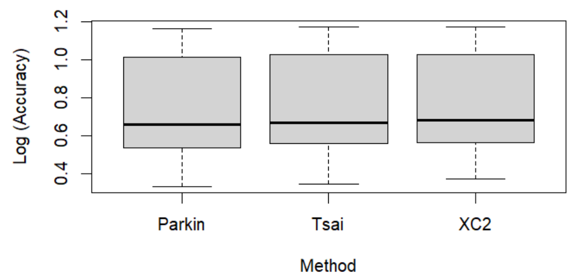

Fig. 7: Accuracy by calibration method (log-scale).

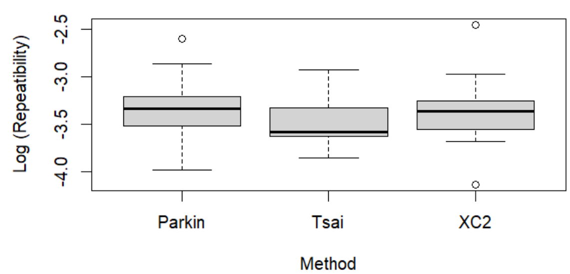

Fig. 8: Repeatability by calibration method (log-scale).

Regarding the calibration methods, Park–Martin shows slightly lower median accuracy values than the remaining approaches (Fig. 7), while Tsai–Lenz exhibits marginally tighter repeatability dispersion (Fig. 8). However, the substantial overlap between distributions indicates that any performance differences are subtle and require statistical confirmation.

The corresponding Type III ANOVA results for the log-transformed metrics are reported in Tables I and II.

Park–Martin achieved the best mean accuracy, Tsai the best mean repeatability, and the Medium illumination condition yielded the best overall metrics, while the complete accuracy and repeatability data can be found in [16].

Prior to hypothesis testing, the normality of the residuals

TABLE I: Type III ANOVA results for accuracy (log-scale).

Factor	**Df**	**Sum Sq**	F **value**	**Pr**$(> F)$
Method	2	0.00324033	22.2833	8.66×10^{-7}
Illumination	2	0.00121359	8.3457	0.001211
Method $\times$ **Illumination**	4	0.00039657	1.3636	0.268423

TABLE II: Type III ANOVA results for repeatability (log-scale).

Factor	**Df**	**Sum Sq**	F **value**	**Pr**$(> F)$
Method	2	0.174907	1.8613	0.17192
Illumination	2	0.198018	2.1072	0.138134
Method $\times$ **Illumination**	4	0.241230	1.2835	0.297053

was assessed using the Shapiro–Wilk test applied to the mixed-effects models. For accuracy (log-scale), the test yielded $p = 0.276$, while for repeatability (log-scale) $p = 0.186$, indicating no significant deviation from normality in either case.

As reported in Table I, both *Method* ($p = 8.66 \times 10^{-7}$) and *Illumination* ($p = 0.00121$) exhibit statistically significant effects on accuracy, whereas their interaction is not significant ($p = 0.268$). In contrast, as shown in Table II, no statistically significant effects are observed for repeatability with respect to *Method* ($p = 0.172$), *Illumination* ($p = 0.138$), or their interaction ($p = 0.297$).

From a statistical standpoint, the absence of a significant Method×Illumination interaction (Tables I and II) indicates that no calibration method exhibits a distinct robustness advantage under specific lighting conditions.

V. Conclusion

This paper presented an experimental comparison of the Tsai-Lenz, Park-Martin, and XC2 hand-eye calibration methods using a fully automated eye-in-hand calibration pipeline for industrial collaborative robots. The proposed workflow integrates intrinsic calibration, extrinsic estimation, and hand-eye computation without human intervention, enabling repeatable and controlled experiments under realistic industrial conditions.

Based on a filtered dataset obtained from 1350 executions conducted under three industrial lighting conditions, the results show that illumination and calibration method both exhibit statistically significant effects on accuracy. No statistically significant interaction between method and illumination was observed, indicating consistent method behavior across lighting conditions. In contrast, neither illumination nor calibration method significantly affected repeatability, suggesting comparable stability among the evaluated approaches.

From a practical industrial perspective, these findings indicate that improvements in automatic hand-eye calibration performance are more closely related to controlling image acquisition conditions than to the selection of a specific calibration algorithm. When sufficient motion diversity and proper experimental conditions are ensured, the evaluated methods present similar repeatability and comparable accuracy levels. The experimental procedure and dataset provided in this work offer a reliable basis for assessing calibration robustness and support the deployment of vision-guided robotic systems in real industrial environments. The complete dataset is available at [16].

References

[1] I. Ali, O. Suominen, A. Gotchev, and E. R. Morales, “Methods for simultaneous robot-world-hand-eye calibration: A comparative study,” *Sensors*, vol. 19, no. 12, p. 2837, 2019. doi: 10.3390/s19122837.

[2] K. Koide and E. Menegatti, “General hand-eye calibration based on reprojection error minimization,” *IEEE Robotics and Automation Letters*, vol. 4, no. 2, pp. 1021-1028, Apr. 2019, doi: 10.1109/LRA.2019.289361.

[3] K. R. S. Santos, E. Villani, W. R. de Oliveira, and A. Dittmar, “Comparison of visual servoing technologies for robotized aerospace structural assembly and inspection,” *Robotics and Computer-Integrated Manufacturing*, vol. 73, p. 102237, 2022, doi: 10.1016/j.rcim.2021.102237.

[4] X. Zhi and S. Schwertfeger, “Simultaneous hand-eye calibration and reconstruction,” in *Proc. IEEE/RSJ Int. Conf. on Intelligent Robots and Systems (IROS)*, Vancouver, BC, Canada, 2017, pp. 1470-1477, doi: 10.1109/IROS.2017.8205949.

[5] A. Tabb and K. M. Ahmad Yousef, “Solving the robot-world hand-eye(s) calibration problem with iterative methods,” *Machine Vision and Applications*, vol. 28, pp. 569-590, 2017, doi: 10.1007/s00138-017-0841-7.

[6] R. Y. Tsai and R. C. Lenz, “A new technique for fully autonomous and efficient 3D robotics hand-eye calibration,” *IEEE Transactions on Robotics and Automation*, vol. 5, no. 3, pp. 345-358, Jun. 1989, doi: 10.1109/70.34770.

[7] Y. C. Shiu and S. Ahmad, “Calibration of wrist-mounted robotic sensors by solving homogeneous transform equations of the form $AX = XB$,” *IEEE Transactions on Robotics and Automation*, vol. 5, no. 1, pp. 16-29, Feb. 1989, doi: 10.1109/70.88014.

[8] I. Fassi and G. Legnani, “Hand to sensor calibration: A geometrical interpretation of the matrix equation,” *Journal of Robotic Systems*, vol. 22, pp. 497-506, 2005, doi: 10.1002/rob.20082.

[9] F. C. Park and B. J. Martin, “Robot sensor calibration: solving AX=XB on the Euclidean group,” *IEEE Transactions on Robotics and Automation*, vol. 10, no. 5, pp. 717-721, 1994.

[10] E. Olson, “AprilTag: A robust and flexible visual fiducial system,” in Proceedings of the IEEE International Conference on Robotics and Automation (ICRA), May 2011, pp. 3400–3407.

[11] ISO 9283:1998, *Manipulating industrial robots — Performance criteria and related test methods*, International Organization for Standardization, Geneva, Switzerland, 1998.

[12] D. C. Montgomery, *Design and Analysis of Experiments*, 10th ed. Hoboken, NJ: Wiley, 2020.

[13] P. I. Corke, *Robotics, Vision and Control: Fundamental Algorithms in MATLAB*, 3rd ed., ch. 13. Cham, Switzerland: Springer, 2023, doi: 10.1007/978-3-031-06469-3.

[14] Z. Zhang, “A Flexible New Technique for Camera Calibration,” *IEEE Transactions on Pattern Analysis and Machine Intelligence*, vol. 22, no. 11, pp. 1330-1334, 2000.

[15] J. Heikkilä and O. Silvén, “A Four-Step Camera Calibration Procedure with Implicit Image Correction,” in *Proceedings of the IEEE International Conference on Computer Vision and Pattern Recognition (CVPR)*, 1997.

[16] F. S. Braga, F. C. Gomes, and W. R. de Oliveira,“Braga_Gomes_Oliveira_CoDIT2026,” GitHub repository, 2026. [Online]. Available: https://github.com/fsbfernando/Braga_Gomes_Oliveira_CoDIT2026